



# Framework proposal for high-resolution spectral image acquisition of effect-coatings

Eva M. Valero<sup>a</sup>, Miguel A. Martínez<sup>a</sup>, Eric Kirchner<sup>b</sup>, Ivo van der Lans<sup>b</sup>, María García-Fernández<sup>a</sup>, Timo Eckhard<sup>a</sup>, Rafael Huertas<sup>a,\*</sup>

<sup>a</sup> Departamento de Óptica, Universidad de Granada, Campus de Fuentenueva, 18071 Granada, Spain

<sup>b</sup> Color RD&I, AkzoNobel Performance Coatings, Sassenheim, The Netherlands

## ARTICLE INFO

### Article history:

Received 22 January 2018

Received in revised form 22 December 2018

Accepted 7 May 2019

Available online 14 May 2019

### Keywords:

Colorimetry

Color measurement

Multispectral and hyperspectral imaging

## ABSTRACT

Hyperspectral imaging of effect coated samples can be challenging, mainly because of the large differences in irradiance that stem from the orientation distribution of the metallic flakes contained in the coating, and from the lightness variations from one sample to another. Besides, high spatial resolution is needed to sample the details of the texture (sparkle) typical of these samples. In addition, focus search strategy and image registration are essential to achieve high quality data for further analysis. In this work, we propose and fully validate a capture framework for measuring spectral reflectance of effect-coated samples with high spatial resolution in 45/0 geometry, using an LCTF (Liquid Crystal Tunable Filter) coupled with a monochrome camera. The main features of the proposed framework are an optimized focus search method based on object movement, a very precise alignment for the images captured in different bands (image registration), achieving sub-pixel accuracy, and a dynamic procedure that uses several white reference surfaces in exposure time estimation to cope with very dark or highly reflective samples. The proposed capture device produces spectral reflectance values comparable to a conventional spectroradiometer using the same observation/illumination geometry, with the additional advantage of achieving a spatial resolution more than two times higher than the human visual system.

© 2019 Elsevier Ltd. All rights reserved.

## 1. Introduction

The term “effect coating” refers to metallic and pearlescent coatings, i.e. coatings containing flake-shaped pigments with a size of several micrometers that are highly reflective and/or show interference. An appealing aspect of the visual appearance of these effect coatings is that the color is not uniform over the coating surface, which is often referred to as visual texture or sparkle, and depends strongly on lighting conditions and viewing angle [1]. Effect coatings are gaining popularity in many fields of application, such as automotive manufacturing, cosmetics and graphics industry [2]. For industrial applications such as color quality control, it is important to accurately measure color properties and color differences between effect coatings, with a high correlation with visual assessment [3]. Since conventional spectrophotometers and spectroradiometers are not able to capture the spatial variation of reflectance properties, multispectral imaging devices may be of

added value, because they can provide spectral reflectance information on a pixel-by-pixel basis.

Nevertheless, only few studies have appeared related to this topic. In a study by Medina et al., Principal Component Analysis is used on hyperspectral images from metallic coatings, as a way to characterize these coatings [4]. Kim et al. use multispectral imaging from pearlescent coatings as a way to characterize angular dependent reflectance and texture functions (BRDF and BTF), thus resulting in a more accurate method for three-dimensional rendering of painted objects [5]. Ferrero et al. analyzed color gamut and color shifts produced when varying observation conditions in effect coatings, using spectroradiometric measurements [6]. Recently, Medina et al. characterized the sparkle of a reduced set of effect coated samples using fractal dimension of the distribution of colors obtained in CIELAB space [7]. Burgos et al. developed a gonio-hyperspectral capture system for automotive paintings, based on LED multiplexed illumination [8]. In previous studies, the main focus was on the analysis of material or texture properties, or building models describing the behavior of the samples under different illumination/observation conditions. Relatively little importance was given to the capture process of spectral data

\* Corresponding author.

E-mail address: [rh Huertas@ugr.es](mailto:rh Huertas@ugr.es) (R. Huertas).

per se, i.e. exposure time and focus settings, complete description of the capture framework and post-processing steps.

Most investigations focused on one of the captured bands and used the same focus settings for all the others [9], or used manual focusing, which is not reproducible [4,7]. Automatic focus search algorithms have been developed for different lens systems and capture devices [10–12], although they were not tested in multi-spectral imaging devices until recently [13]. In previous studies, the exposure time was usually set for the effect coated sample and the same exposure was used for the reference white used to obtain spectral reflectance. This poses prospective problems for very dark or very light samples, as we will illustrate in this work. However, we have not found any mention about these limitations in previous studies, very likely because a restricted set of selected samples was used.

The significant difference in radiance between sparkles and background can cause problems when attempting to find the correct exposure. For many samples, the metallic flakes, which produce the texture effect, are oriented randomly, and the camera unavoidably captures specularities that increase the dynamic range in the scene. Besides, the different substrates can vary from very dark to very light for different samples, and the capture system should cope with this variability as well.

In this context, high-resolution images are promising for enabling exhaustive texture analysis. Thus, usually a relatively short distance between camera and sample is used, and this can accentuate both the problem of defocus for some bands when only one focal position is used for all of them, and misalignment caused by the residual chromatic aberration of the lens. In addition, for accurate measurements care must be taken to ensure that the focal settings are reproducible for the sample and the white reference captures. We should point out that in previous studies there was no mention of the registration of the images captured in different spectral bands. Besides, if the different bands are not properly aligned (registered), some artifacts such as color fringes or blurring may occur in a color-rendered spectral image when very small objects (e.g. metallic flakes) are imaged at short distance from the camera lens.

Summarizing, a poor capture workflow design can be a critical limitation for measuring spectral reflectance of effect coatings. Particularly, some care should be taken to avoid problems with the exposure settings, focus and registration of the images at different spectral bands. In the current study, we propose a novel workflow for high-resolution spectral image acquisition, based on the usage of a liquid-crystal tunable filter (LCTF), and specifically aimed at samples of effect coatings, with the purpose of overcoming the previously mentioned limitations. We propose an optimal focus search strategy based on object movement instead of lens movement, together with an accurate registration of the images in the different spectral bands, and an improved exposure-time estima-

tion procedure, which can cope with the high dynamic range problem caused by very dark or very light base pigments, or by the orientation of metallic flakes, and/or by significant absorption in some wavelength bands, for example when highly saturated colors are used as base pigments.

The paper is organized as follows. In Section 2 we describe aspects of the spectral image acquisition method, such as the opto-mechanical set-up and the acquisition procedure. We discuss the acquisition process in detail, describing also how optimal exposure time is estimated, and how optimal focus position search is carried out. In Section 3 we describe the image post-processing and image registration procedures, and the method for obtaining the spectral reflectance factor image. In Section 4 we describe several experiments designed to test and evaluate the proposed set-up and framework. Besides, as a direct application of the proposed framework, we evaluate the spectral and color accuracy as compared to conventional instrumental approaches for color measurement. The main conclusions from this investigation are summarized in Section 5.

## 2. Spectral image acquisition

### 2.1. Opto-mechanical set-up

The set-up for image capturing that we developed is formed by the following elements, as shown in Fig. 1:

- (a) Monochrome camera model Retiga SRV, by QImaging Ltd, Canada. The  $2/3''$  sensor captures images with 12 bit intensity resolution, a spatial resolution of  $1392 \times 1040$  pixels, and has a pixel size of  $6.5 \times 6.5 \mu\text{m}$ .
- (b) Navitar Zoom 7000 Lens, with a focal range of 18–108 mm. We set the focal length to 108 mm to achieve high spatial resolution in the captured images. The lens aperture was set to the intermediate position in the aperture wheel of the lens.
- (c) Liquid Crystal Tunable Filter (LCTF) model Varispec VIS-10-20, from Perkin Elmer Corp., US. The filter can be tuned to wavelengths from 400 to 720 nm, with a 10 nm bandwidth. It has a 20 mm wide aperture, with an angle of acceptance of  $7.5^\circ$ . We captured spectral images in the range from 400 nm to 700 nm, with a sampling interval of 10 nm (31 bands). The filter was attached directly to the Navitar Lens with a special adapter to avoid stray light.
- (d) Linear Stage with sample holder. A sample holder was mounted on a motorized linear stage Model LTM 80–100, by OWIS GmbH, Germany. The linear stage has a travel distance of 95 mm, with maximum speed of 1 cm/s and positioning error less or equal than  $25 \mu\text{m}$ .

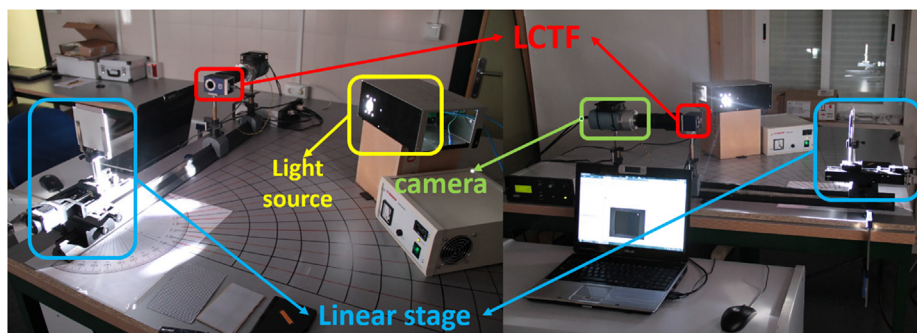


Fig. 1. Opto-mechanical set-up.

(e) Xenon Lamp Cermx PE300BFA by Excelitas Tech Corp, US, driven by a power source model XL2000, by Perkin Elmer Corp., US. The lamp emits 50 W radiant total output, with a peak intensity of 515000 cd, 300 W input electrical power, and a beam opening half-angle of 6°. Fig. 2 shows the Spectral Power Distribution (SPD) of this light source, measured by a PhotoResearch Spectrascan PR-745 spectroradiometer, using a reference white SphereOptics Zenith Lite of 95% reflectance.

The illumination/observation geometry for all measurements is with the lamp oriented at an angle of 45° with respect to the plane of the sample holder (see Fig. 1), while the LCTF, lens and camera were placed at 0° observation geometry to resemble most closely the standard CIE 45/0 illumination/observation geometry, recommended for spectral reflectance measurements [14].

## 2.2. Acquisition procedure

### 2.2.1. Overview of the proposed acquisition work-flow

The work-flow consists of two main procedures: a calibration step in which optimal exposure time and focus positions are determined for each spectral image band, and a capture step, in which spectral image cubes are captured. The block diagram in Fig. 3 shows the capture procedure including the calibration step and the capture step.

In the calibration step, the main reason for the need of focus position search at each spectral band is chromatic aberration, which produces un-sharp images for different spectral bands, unless they are correctly focused and aligned (registered). Exposure time estimation and optimal focus position search do not require storing the acquired spectral cubes, but only optimal exposure time and focus position settings. This calibration data remains

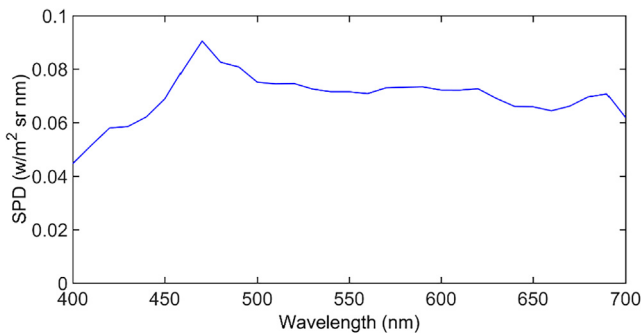


Fig. 2. Spectral Power Distribution of our light source (Cermx Xe Lamp PE-300BFA).

valid unless there are significant changes in the lamp spectral power distribution, or mechanical changes introduced in the set-up that affect the relative distances between the light source and the sample holder and/or the camera and the sample holder.

In the capture step, several image cubes are acquired: a dark cube to perform dark image subtraction, a white reference cube for performing flat-field correction (as explained in Section 3.1), a geometrical calibration cube, which consists of a checkerboard pattern printed on white paper, to be used for registration purposes, and finally the sample cube. In the white reference, geometrical calibration and sample cubes' capture, the optimal exposure times and focus positions, previously determined in the calibration step, are used. We do not use the optimal focus positions for acquiring the black cube, since the aperture is closed during its capture.

### 2.2.2. Exposure time estimation

For estimating the exposure time in the calibration procedure, we initially used a Color Checker Passport reference white (X-Rite, US). Additionally, we also used two more reference surfaces for a modified exposure time estimation procedure for very dark or very light samples, which will be explained below. For each spectral band, we implemented a simple iterative procedure that relies on the assumption that the camera response is linear with exposure time. This assumption holds acceptably well for our set-up conditions, since we avoided the upper and lower portions of the total range of camera responses for the captures used in exposure time estimation. This was done to prevent either saturated or underexposed pixels appearing in the area of interest for the capture.

We set the initial exposure time,  $t_i$ , for the 400 nm band to 30 s, a value heuristically found to be suitable to our acquisition conditions, and which did not compromise the linearity of the camera responses with exposure time. Then, we acquired an image with this initial exposure time, and computed the mean camera response value  $C_m$  of a manually selected central Region of Interest (ROI) in the captured image. A target camera response  $C_t$  was set at 80% of the maximum of the response range, i.e.  $C_t = 0.8 (2^{12} - 1)$  for a 12-bit camera. As shown in Eq. (1),  $C_m$  is compared with  $C_t$  with a tolerance range, set at  $\pm 2\%$ , i.e.  $0.02 (2^{12} - 1)$ :

$$\text{if } C_m \in [C_t \pm 0.02(2^{12} - 1)] \Rightarrow t_e = t_i; \text{ else } t_{i+1} = \frac{C_t}{C_m} t_i \quad (1)$$

where  $t_e$  is the current exposure time, and  $t_{i+1}$  is a new exposure time estimated in iteration  $i$ . The exposure time estimation procedure runs until  $C_m$  is within the tolerance range or  $t_e$  exceeds 30 s. This is to avoid very long exposure times and non-linearities of the camera.

Following the iterative process of successive exposure time estimation and image acquisition, exposure times are found for each

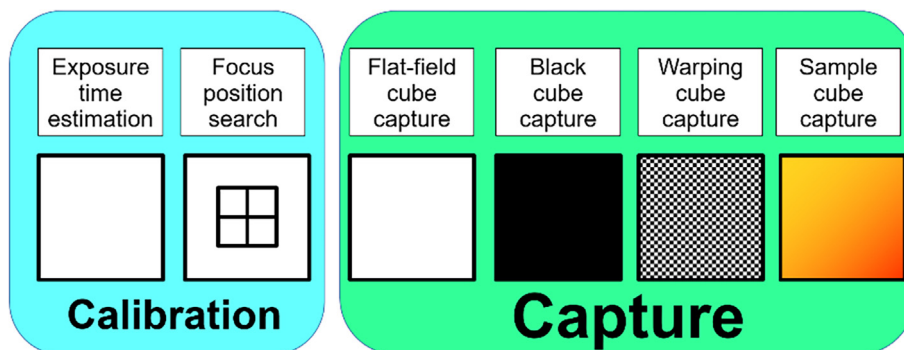
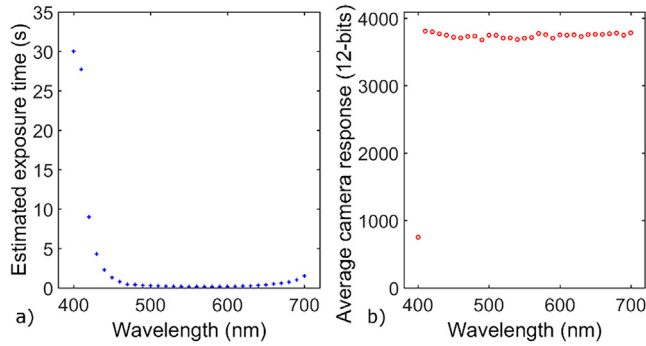


Fig. 3. Block diagram of the capture process including the calibration and capture procedures.



**Fig. 4.** (a) Exposure time distribution for a typical capture, as a function of wavelength. (b) Average signal of the white reference cube in a  $500 \times 500$  pixels central portion of the image. At the 400 nm band, the exposure is set at 30 s (maximum value allowed). Even with this setting, the signal in the ROI does not reach the required  $C_t$  level.

spectral band, while adjusting the initial exposure time to the previous image band as a first guess.

Fig. 4a shows estimated exposure times in a typical capture as a function of central wavelength of each band. We can observe that the exposure time curve is concave, with a central minimum and increasing values for short, and in a lesser degree, for long wavelengths. This is expected, given that the camera and lens responsivity, LCTF transmittance and the light source SPD (Fig. 2) are at their lowest in the extremes of the wavelength range. It can also be seen that for the 400 nm band the maximum exposure time of 30 s was reached (see Fig. 4a), without the signal of the white reference reaching its target value ( $C_t$ ) as shown in Fig. 4b.

It was further observed that the image intensity was not evenly distributed within the selected ROI, which can be explained by the spatial non-uniformity of the illumination. Consequently, values larger and smaller than  $C_m$  occur in the ROI. Nevertheless, saturation could be prevented in the ROI regardless of the spatial non-uniformity because we set  $C_t$  to 80% of the maximum camera response.

For a typical capture, the exposure time estimation step takes approximately 3 min (about 8% of the total capture time).

Since our exposure time estimation procedure is based on imaging the white reference surface, it could lead to either saturation or underexposure for samples, or regions within the samples that are much lighter or much darker than the white reference. To avoid saturation, a very straightforward alternative solution would be to use a reference white with higher reflectance values. We have tried this modification introducing the SphereOptics white reference mentioned in Section 2.1 as reference white. However, while it solved the problem of saturation, it also resulted in lower camera response values for all samples and increased the underexposure problem for the darker ones, yielding images with potentially unusable data due to the low signal-to-noise ratio. The main problem with the design described before stems from the high dynamic range considering the full set of sample scenes as well as the white reference scenes.

To solve this problem, we have introduced an adaptive procedure for exposure time estimation, which is able to cope with this dynamic range problem by changing the white reference to improve the match between sample and white radiance signals, at the cost of increasing the temporal duration of the calibration step of the work-flow. We have called this procedure *dual reference dynamic exposure time setting*. It consists in using two different reference surfaces, and three different values of target camera response value ( $C_t$ ) for the exposure time estimation. In this way, we dynamically select the reference surface and the signal level which produces camera response values that are neither saturated

nor underexposed for a given sample and spectral band. To implement it, during the calibration procedure, we run the exposure time estimation algorithm six times, combining 2 reference surfaces with 3 target response values. The three target response values considered are 80%, 50%, and 20% of the maximum camera response value (3276, 2048, and 819 respectively for a 12-bit camera). The two reference surfaces are the SphereOptics white, and the dark grey (sample 23) of the X-Rite Color Checker 24. Thus, we obtain six white reference cubes and six different exposure times for each capture band.

During the acquisition procedure, first an image is captured with the central exposure time of the six available from the calibration procedure for each band. If the averaged camera response value of a manually selected ROI ( $C_m$ ) contained in this image is below 15% or above 85% of the maximum value (4095 digital counts for a 12 bit camera), the exposure time is considered unacceptable. Thus, different exposure times are subsequently selected from the six available, either increasing or decreasing the initial exposure time, until we obtain average camera responses that fall within the acceptable range. Then, the image is captured with this exposure time and the procedure is applied to the next band. Afterwards, the image for each band is processed with the corresponding reference white image for the band, i.e. the reference white image captured with the same exposure time.

The results of an experiment which validates this adaptive exposure time estimation procedure are presented in Section 4.3.

### 2.2.3. Optimal focus position search

As explained previously (see Sections 1 and 2.2.1), one of the main novel features of our acquisition setup is the focus strategy, which is achieved by moving the sample rather than by conventional lens focusing, and is applied for each spectral band. The method used can be classified into the category of *passive focus-position search methods*, in which image quality (sharpness-related) real-time measurements are used as cost function to determine the best focus position [15]. We have chosen this focus setting strategy because linear stages allow for very precise and reproducible movements, and are less costly than autofocus zoom lenses with the features required in our application.

As described in [16], a typical passive focus-position search algorithm is composed of two main procedures: the building of the Focus Measurement (FM) curve, in which sharpness-related measurements are obtained for candidate focus positions, and the Focus Search (FS), in which the best candidate is selected. The FS procedure determines how the candidate focus positions are chosen, and so influences the FM curve building process, particularly, the temporal duration of this procedure, which is critical for cases when the exposure time is relatively long.

For the building of the FM curve, we selected a commonly used sharpness index,  $S$ , computed as the cumulative sum of the squared modulus of the gradient of the image [17]:

$$S(I) = \frac{1}{hv} \sum_{ij} [(G_x(i,j))^2 + (G_y(i,j))^2] \quad (2)$$

where  $h$  and  $v$  are image height and width respectively for a manually selected central ROI of image  $I$  (which includes a focus target pattern),  $i = 1, \dots, h$ ;  $j = 1, \dots, v$ , and  $G_x, G_y$  are the horizontal and vertical gradient vector components.

The focus pattern consists of nine rectangles printed with black toner, with low reflectance over the entire visible range of the spectrum (see Fig. 5).

Our FS algorithm makes use of the Golden Section Search procedure (GSS, [18]), a well-known numerical extrema location technique. The GSS algorithm inserts new points in the FM curve ensuring that they are as equally spaced as possible from previous



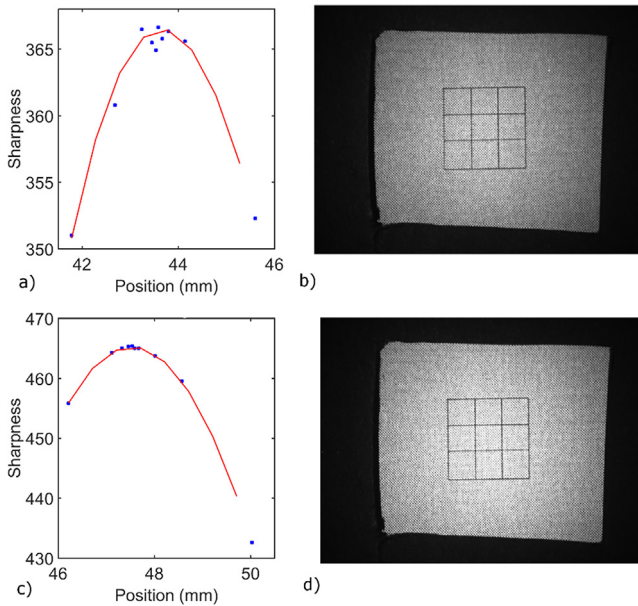


**Fig. 5.** Typical GSS FM curve and polynomial fitting for band (a) 410 nm, (c) 420 nm. In the vertical axis, we see the sharpness metric, and in the horizontal axis, the linear stage position in mm. The figures (b) and (d) show the focusing target at the optimal focus position found.

values of the search range. Our FM curve represents sharpness as a function of linear stage position. Initially, images are acquired at the starting position ( $X_i$ ), and the extremes of the search interval placed at  $X_L = (X_i - 5)$  mm and  $X_H = (X_i + 5)$  mm. Then, we narrow the search interval by updating the extremes of the search range (which will be called  $X_{L,i}$  and  $X_{H,i}$ , where  $i$  is the iteration number) based on the parameter  $\tau$  computed as shown in Eq. (3):

$$\tau = \frac{\sqrt{5} - 1}{2} \quad (3)$$

For the first iteration,  $X_{L,1}$  and  $X_{H,1}$  are computed as:

$$\begin{aligned} X_{L,1} &= X_L + (1 - \tau)(X_H - X_L) \\ X_{H,1} &= X_L + \tau(X_H - X_L) \end{aligned} \quad (4)$$

And two new images are captured. Then, in each successive iteration,  $i$ , the start and end positions of the search interval are updated following this rule:

$$\begin{aligned} &\text{if } S(X_{L,i}) > S(X_{H,i}) \text{ then} \\ &\{X_{L,i+1} = X_L + (1 - \tau)(X_{H,i} - X_L); X_{H,i+1} = X_{L,i}\} \\ &\text{else } \{X_{L,i+1} = X_{H,i}; X_{H,i+1} = X_{L,i} + \tau(X_H - X_{L,i})\} \end{aligned} \quad (5)$$

This process is repeated until the search range  $|X_{H,i+1} - X_{L,i+1}|$  is less than 0.25 mm, or 30 iterations are reached.

A polynomial curve is then fit to the FM curve and evaluated at its maximum. The focus position corresponding to this maximum is considered optimal for the given spectral band.

Fig. 5 shows two instances of FM curves with their corresponding polynomial fits. We can appreciate the typical GSS irregular spacing of the search positions (blue squares in Fig. 5). For Fig. 5a, in spite of the FM curve not being smooth, we still can locate a satisfactory optimal focus position using the polynomial fitting step. In other cases, the FM curve is closer to the fitted polynomial, as in Fig. 5b.

Since we are capturing a hyperspectral image, we need to run the focus position search procedure for each band of the hyperspectral image. The process is as follow: We first set the LCTF wavelength to a central position (560 nm) and capture an image

using the exposure time estimated previously for this band. Then, if the image looks un-sharp we adjust manually the focus of our camera lens to be able to select the ROI for the focus search. Afterwards, we run the GSS looping over all the bands. The GSS starting position ( $X_i$ ) for each band is either taken from a previous set of optimal focus position data, or, if no previous data were available, set to the middle position of the step motor (50 mm).

For a typical capture, the optimal focus position step with GSS takes around 24 min (60% of the total time including the calibration and capture procedures).

In Section 4.1 we present some validation experiments for our FS algorithm, and show running time and sharpness values reached when we compare with other FS procedures.

### 3. Image post-processing

In this section, we describe how the cubes acquired during the capture procedure are used to correct the spatial inhomogeneity of the illumination, the dark current signal level of the camera, and the misalignment between different spectral bands; illustrating thus in detail the process of obtaining the final spectral reflectance factor image cube for a given sample.

#### 3.1. Flat-field correction, dark image subtraction and reference reflectance normalization

In order to recover the spectral reflectance information of the imaged samples, the SPD of the illumination (Fig. 2) has to be discounted, as well as the spectral sensitivity of the imaging system, and the spatial inhomogeneity of the illumination. This can be achieved in a single step by flat field correction, since we are capturing narrow spectral bands.

There are several sources of noise in an imaging system [19,20]. Among others, the impact of two of the most important ones, the dark current noise and the thermal noise, can be discounted by subtracting the so-called dark image, obtained by completely blocking the light impinging in the sensor.

The flat field correction and dark image subtraction are performed as described in Eq. (6):

$$\text{Sample}_{\text{corrected}}(x, y, \lambda) = \frac{\text{Sample}(x, y, \lambda) - \text{Dark}(x, y, \lambda)}{\text{White}(x, y, \lambda) - \text{Dark}(x, y, \lambda)} \text{Refl}_{\text{white}}(\lambda) \quad (6)$$

where  $\text{Refl}_{\text{white}}$  is the known reflectance of the white reference sample used, and *Sample*, *Dark* and *White* are the images of band  $\lambda$  for the cubes captured during the acquisition procedure.

If the *dual reference dynamic exposure time setting* is used for exposure time estimation, then we use the corresponding reference image (previously stored in the calibration procedure) to perform the flat field correction of Eq. (6).

#### 3.2. Image registration

Within the domain of multispectral imaging, registration can be defined as the procedure aiming to align spatially each image in the captured cube to a given reference image, which usually is one of the bands [21]. This essentially means that one of the bands, called reference band, (550 nm in our case) is unchanged by the process, while the rest of the bands are spatially transformed to achieve alignment on a pixel-by-pixel basis with this reference band. The required transformation is not the same for all bands, which means that we have to solve  $N-1$  individual registration problems, with  $N$  being the number of captured bands.

To register correctly each band with the reference image, we need to model the displacement pattern between the unregistered

and registered images, and then move the pixels in the unregistered image to the “correct” location in which the reference band corresponding pixel is placed. Then, the problem can be solved for each band with a transformation in the spatial domain, usually followed by image re-sampling, since the displacements found are not necessarily integer values.

In registration problems, it is fairly important to have some previous knowledge about the type of distortions that could be present [22]. In Multispectral Imaging applications, often the distortions are caused by camera or object movements along the capture of the different bands, or geometrical aberrations of the lens. In such cases, the registration problem can sometimes be solved by finding a global transformation, i.e., a transformation that is applied globally to all pixels in the unregistered image. In our case, distortions vary locally across the image. Besides, we aim for a very accurate registration result. Thus, we need to find a model for the image transform that can be different for different parts of the image, i.e. local transforms. Local transforms [23] are necessarily slower to apply and some care must be taken to stitch the different local functions seamlessly, to avoid causing artifacts in the registered image. One way to apply local polynomial transforms is to use a non-rigid model based, for instance, on B-splines interpolation techniques with local support [24].

The main causes of image misalignment for our image data are lens distortion, lens chromatic aberration, and a global image displacement resulting from moving the sample along an axis that is not the optical axis of the imaging system during the acquisition. This last problem can be reduced by careful setup, but, in practice, it is very hard to avoid entirely. These three factors combined result in local variations of the pixel displacements for each band with respect to the reference band. In addition, a slight tilting of the LCTF filter, in combination with the lens geometrical aberration, may cause local distortions as shown in [25] for a filter wheel multispectral system. Finally, the use of quasi-monochromatic light in spectral imaging can produce more noticeable effects of the chromatic aberration naturally occurring in the captured images.

We have recently proposed a solution to a non-rigid registration problem for a Hyperspectral Imaging system based on Bragg gratings (V-EOS, Photon Etc., Canada) [26], using a free-form deformation model of multilevel refined uniform cubic B-splines. The method works by tracking the displacement of some key pixels in the scene, extracted from a checkerboard pattern, and fitting a B-splines model to the displacement field. We obtain the displacement value at any given pixel position by interpolation of the fitted model displacement surface. We have adapted this technique to our acquisition workflow, using a geometrical calibration cube

(checkerboard pattern formed by squares of 1.66 mm) acquired in the capture process.

In Fig. 6, we show the overlap of a zoomed area of the bands 430 nm and 550 nm, before (a) and after (b) the registration post-processing is applied. The before registration image was processed with Matlab to show the misalignment effect in an intuitive way. We can clearly observe such effect along the edges of the checker pattern sample, and how it is corrected after registration.

In Section 4.2 we will show quantitative results of an experiment performed to evaluate the registration accuracy obtained using this method in our image acquisition process.

## 4. Experiments

### 4.1. Optimal focus position search algorithm evaluation

In this section, we describe an experiment aiming to validate the proposed GSS-based optimal focus position search procedure. We evaluate the maximal sharpness reached and total running time of the search procedure.

We compare the GSS optimal focus position algorithm with two other approaches: the first one is not performing focus position search at all, called “Nothing” condition. The second one is running a more exhaustive search procedure in two steps, called “Coarse to Fine” (C2F) condition.

In the C2F algorithm, the sharpness is computed at equally spaced focus positions, using the same starting point as in the GSS algorithm. The first step, Coarse Search, takes seven images from  $(X_i - 15)$  mm to  $(X_i + 15)$  mm sampling at 5 mm steps, where  $X_i$  is the starting position. After the images are captured, the FM curve is fitted with a third degree polynomial, and the position for maximum sharpness is found. This position is used as the starting position for the second step of the algorithm, Fine Search, in which the sharpness is measured for another seven images from  $(X_i - 1.5)$  mm to  $(X_i + 1.5)$  mm, sampling at 0.5 mm steps. Then, another cubic polynomial is fitted to the data, and the maximum sharpness value and optimal focus position is obtained from this second FM curve, which has been sampled more finely at 0.5 mm intervals. Thus, in total the C2F method requires capturing 14 images for each band.

To evaluate the performance of the three approaches, we captured an image cube with the focus target on the sample holder (see Section 2.1 and Fig. 3 for a description of this target) using the optimal focus positions found for GSS and C2F algorithms. To test the ‘Nothing’ approach, we acquired a cube using a fixed object plane position corresponding to the starting point of GSS and C2F for the 560 nm band.

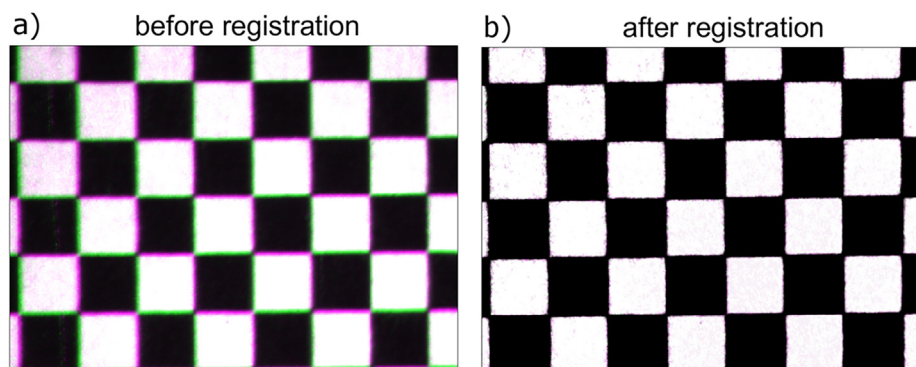


**Fig. 6.** Overlap plot of a zoomed-in area of bands 430 nm (shown as green and black image) and 550 nm (purple and black image). (a) before registration and (b) after registration and post-processing. (For interpretation of the references to color in this figure legend, the reader is referred to the web version of this article.)

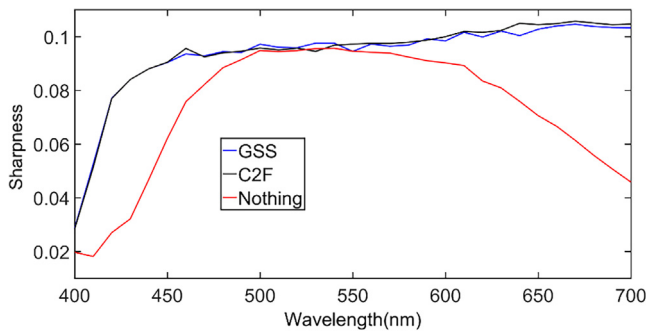


**Fig. 7.** Sharpness in the ROI as a function of wavelength, for the captured focusing target cubes in the three conditions tested.

Then, we measured the sharpness in a ROI, which was the same for each cube, once the cubes were post-processed to ensure correct alignment of all pixels within this ROI for all the bands. In Fig. 7, we show the sharpness as a function of wavelength, evaluated for the three approaches. Please, note that the scale of sharpness values is different than in Fig. 5 because for Fig. 7 we have used post-processed cubes, so the range of image intensity values is [0,1], and the sharpness value depends on image intensity. This does not pose any problems for the FS strategy proposed in this study, since we evaluate sharpness independently for each band in different object positions, and all images compared have a very similar intensity distribution. From the results in Fig. 7, we can point out several interesting observations:

- The “Nothing” condition results in a steep decrease in sharpness in the bands far from the 560 nm reference. These images are unacceptably blurred and would provide useless data for further analysis. The results pinpoint the need for using a FS strategy within our capture framework.
- Both GSS and C2F algorithms provide very similar sharpness at the focus positions found.
- The lowest sharpness is found for the 400 nm band in all three conditions. We can explain this by the fact that the optimal exposure was longer than 30 s (maximum exposure time set within our capture framework). Therefore, the optimal signal value ( $C_i$ ) was not reached for this band (see Fig. 4), and the images were somewhat underexposed, resulting in lower intensity values and so lower values of the sharpness metric. This does not mean that the images are more blurred for 400 nm, only that the sharpness metric, which is intensity dependent, has a different scale for this band. We could overcome this problem by setting a higher

**Table 1**  
Running time of C2F and GSS algorithms.

| Algorithm | Running Time (s) | Percent of total capture time for calibration capture | Percent of increase in time in the Focus Search step |
|-----------|------------------|---|--|
| GSS       | 1297.70          | 60.30   | 0  |
| C2F       | 3097.58          | 57.42   | 238.7  |

exposure time limit, but this would cause a significant increase in the capture time, and also potential failing of the linearity of the camera response with received radiance.

As we can see from Figs. 5 and 8, the sharpness reached by both GSS and C2F algorithms is satisfactory, no blurring being visually perceptible in the images captured at the Optimal Focus Positions found. The main difference between GSS and C2F is found when we evaluate the performance in terms of running time (see Table 1). C2F running time is higher by approximately a factor of 2.4 compared to GSS, while providing similar optimal sharpness results. The percentage of total acquisition time taken by the FM step is similar for both algorithms, around 60%. This points out the importance of saving time in the FS step of our proposed framework. In total, GSS took 21 min 38 s, while C2F took 51 min 38 s, representing a considerable amount of time saved in the calibration procedure.

If we examine the difference in the Optimal Focus Positions found by C2F and GSS in all the bands tested, we find in average 0.85 mm (with standard deviation of 0.21 mm). GSS tends to find positions slightly closer to the camera in all bands. These differences in position do not result in perceptible variations in sharpness. We think these differences lie within the depth of field of the camera, since the sharpness results are reflecting the fact that the images are equally sharp in both C2F and GSS optimal focus positions.

#### 4.2. Evaluation of registration performance

We have evaluated the performance of the registration step of the proposed framework by using a metric based on displacement statistics of the geometrical calibration cube. We take as reference the spatial coordinates of all corners extracted in a central section of  $15 \times 11$  squares of the checkerboard pattern from the reference band (550 nm). Then, for each band, we extract corresponding corners, and compute the difference in x and y pixel coordinates positions with respect to the reference band. The 192 ( $16 \times 12$  corners) element vectors (two x and y displacement vectors for each of the 32 bands) are then analyzed in terms of first order statistics.

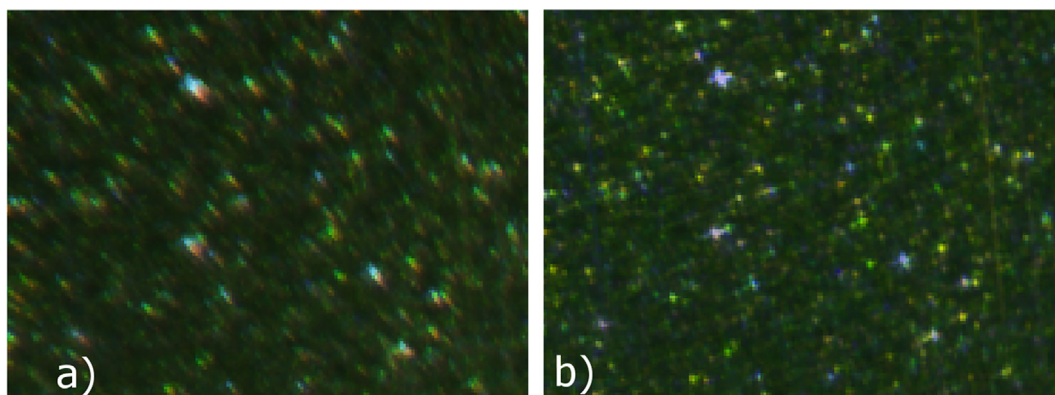


**Fig. 8.** RGB rendered image of an effect coated sample before (left) and after (right) applying the post-processing steps.



**Table 2**  
Fitting and alignment error for x and y coordinates.

|                     | 1 (Before registration) | 2 (Fitting error) | 3 (Alignment error) |
|---------------------|-------------------------|-------------------|---------------------|
| <i>x coordinate</i> |                         |                   |                     |
| Mean                | 1.4872                  | 0.2146            | 0.6644              |
| STD                 | 1.6992                  | 0.1963            | 0.6982              |
| Max                 | 10.4466                 | 1.8039            | 3.9465              |
| 95 Percentile       | 3.5475                  | 0.6018            | 2.2706              |
| <i>y coordinate</i> |                         |                   |                     |
| Mean                | 1.4805                  | 0.1721            | 0.1796              |
| STD                 | 1.4922                  | 0.1532            | 0.1819              |
| Max                 | 7.8392                  | 1.4398            | 2.2518              |
| 95 Percentile       | 4.7806                  | 0.4700            | 0.497               |

In this experiment, for comparison, we have obtained the displacement vectors in three conditions:

- 1) Before performing registration.
- 2) After performing registration, from the same cube used to compute the registration transformation. We call this the “fitting” error.
- 3) After performing registration, from a checkerboard target cube acquired later on, but corrected by the previously obtained registration transformation. We call this the “alignment” error.

All the cubes captured in conditions 1, 2 and 3 share the same optimal focus positions. Please, note that the registration transformation is only valid for a particular set of focus positions and has to be refitted once these positions change.

Table 2 shows the first order statistics corresponding to the fitting and alignment error displacement vectors for x and y coordinates in the three conditions described above. We can see that we reach sub-pixel registration accuracy for the fitting error, reducing the average displacement to around 0.2 pixels in both x and y coordinates. Both average and 95 percentile of the displacement vectors are below 1 pixel, and the maximum value is of the same order as the average displacement in condition 1 (before registration). The alignment error is clearly higher than the fitting error, at any rate for the x coordinate and less clearly for the y coordinate. This might reflect a tendency to overfitting of the registration model, which is not worrying because we still reach on average sub-pixel accuracy in the alignment error.

In Fig. 6, we show the overlap of the reference (550 nm) and 430 nm bands in condition 2. The rest of the bands show the same behavior, also in the cube used in condition 3.

Fig. 8 shows a zoomed-in area of a sample cube before (left) and after (right) the post-processing procedure was carried on. The spatial details are enhanced, and the sparkle color can be analyzed without the artifacts produced by the misalignment and defocus effects that appear in the left part of the Fig. 8.

Thus, we can conclude that registration is performed accurately in our framework.

#### 4.3. Evaluation of spectral and color accuracy

In this section, we describe two experiments performed to test the spectral and colorimetric accuracy of the proposed device and the acquisition work-flow for measuring the spectral reflectance of different types of planar samples, comparing with conventional instrumental approaches for color measurement.

In both experiments, the spectral reflectance of the samples was computed over a ROI of 500x500 pixels, roughly equivalent to  $1.7 \times 1.7^\circ$  of viewing angle subtended from the center of the LCTF. We also measured the spectral reflectance of the samples with two other devices operating in different illumination/observation con-

ditions. The first device was a PR-745 spectroradiometer from SpectraScan (US), operating with  $2^\circ$  field of measurement. We averaged 5 spectral radiance measurement cycles to obtain the corresponding data for sample and reference white. The second device was a Minolta CM-2500d spectrophotometer, operating with d/8 geometry and with a measurement area spot of 10 mm. We are aware that the differences in geometry between PR-745 and CM-2500d devices do not allow direct comparison of the measurements, but we introduce the spectrophotometer results as a way to show the upper limit of inter-instrument differences that we can expect for our set of samples.

For both experiments, two sets of samples have been considered.

- (a) *The solid set*, in which a flat metal substrate is covered by a high-gloss coating, consisting of conventional absorption pigments. The color of these samples is completely visually uniform. Therefore this set is used as a reference set for which the measurements provided by spectral imaging are expected to correlate well with point-measurement devices (eg. PR-745 and CM-2500d).
- (b) *The effect set* contains samples with a variety of paints typical for different coating markets: powder coatings, architectural coatings for metal substrates, and coatings for the car repair industry and consumer electronics. The color of these effect samples is not uniform, as it varies at a spatial scale that differs for the various samples. In addition, the gloss level varies over this set of samples. Many of these coatings contain metallic and/or pearlescent flake-shaped pigments. Depending on the lighting conditions and viewing angle, sparkle or coarseness patterns are visible to a varying extent.

The first experiment was performed on samples that do not contain very dark or light base pigments, considering 9 samples from the solid set and 17 samples from the effect set.

For the second experiment, we chose 7 *solid* and 21 *effect* samples which resulted in extreme lightness values when viewed in our observation/illumination conditions. The spectral images of these samples were captured using the *dual reference dynamic exposure time setting*, specifically developed for these samples, as described in Subsection 2.2.2.

##### 4.3.1. Comparison metrics

In the experiments described in this section, we used one colorimetric and two spectral indices to determine the degree of inter-instrument agreement. The spectral metrics are the Goodness-of-Fit coefficient (GFC), related also to the Pearson Distance [27], and the Root-Mean-Square Error (RMSE). The colorimetric index is the CIEDE00 color difference formula [28]. For spectral indices, it is generally accepted that a GFC over 0.999 and RMSE below 0.02 give a reasonable degree of closeness between two reflectance measurements, although the criterion to determine an acceptable match between samples might depend on the particular application for the spectral data [29].

##### 4.3.2. Experiment 1: solid and effect coated samples not containing extreme lightness values

Fig. 9 shows the spectral reflectance values measured by the three devices for two samples, which RMSE (a and b) or CIEDE00 differences (c and d) are near to the 95 and 5 percentiles in the respective distributions, as representative examples of the set used in Experiment 1.

Table 3 shows first order statistics of the spectral and color metrics used to compare the three measurement devices. From this data, we make the following observations and conclusions related to inter-instrument differences:



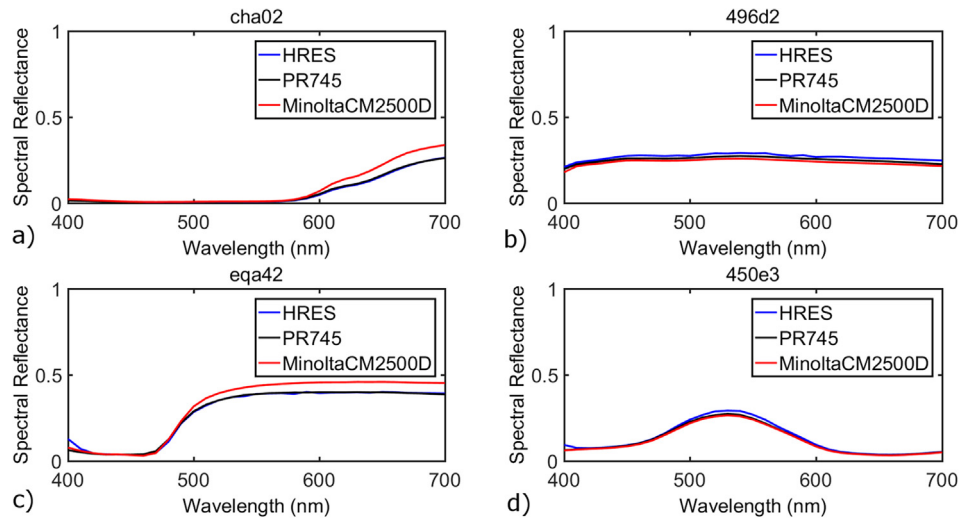


**Fig. 9.** Spectral reflectance factor for a sample with RMSE close to the 5 percentile (a), RMSE close to the 95 percentile (b), CIEDE00 close to the 5 percentile (c) and CIEDE00 close to the 95 percentile (d) in the comparison between HRES and PR745 measurements for Experiment 1 in Section 4.3.

**Table 3**

First order statistics for normal samples (Experiment 1).

|               | HRES-PR745 |        |        |         | HRES-MINOLTACM2500D |        |         |         | PR745-MINOLTACM2500D |        |         |         |
|---------------|------------|--------|--------|---------|---------------------|--------|---------|---------|----------------------|--------|---------|---------|
|               | RMSE       | GFC    | CIELAB | CIEDE00 | RMSE                | GFC    | CIELAB  | CIEDE00 | RMSE                 | GFC    | CIELAB  | CIEDE00 |
| Mean          | 0.0094     | 0.9996 | 1.844  | 1.130   | 0.0357              | 0.9991 | 5.679   | 3.785   | 0.0309               | 0.9995 | 5.138   | 3.341   |
| Median        | 0.0078     | 0.9997 | 1.790  | 1.130   | 0.0252              | 0.9997 | 4.012   | 2.748   | 0.0156               | 0.9999 | 3.284   | 1.952   |
| STD           | 0.0052     | 0.0003 | 0.898  | 0.529   | 0.0405              | 0.0014 | 4.455   | 2.695   | 0.0400               | 0.0010 | 4.600   | 2.829   |
| Max           | 0.0222     | 1.0000 | 4.1034 | 2.4814  | 0.1956              | 1.0000 | 18.2274 | 10.9527 | 0.1829               | 1.0000 | 18.5782 | 9.7252  |
| Min           | 0.0023     | 0.9990 | 0.3467 | 0.3202  | 0.0041              | 0.9945 | 0.1377  | 0.0947  | 0.0034               | 0.9953 | 0.6502  | 0.4017  |
| 95 Percentile | 0.0164     | 1.0000 | 3.1509 | 1.9109  | 0.1071              | 0.9999 | 15.2573 | 8.4248  | 0.1060               | 1.0000 | 14.0018 | 8.3680  |
| 5 Percentile  | 0.0028     | 0.9991 | 0.4363 | 0.3559  | 0.0059              | 0.9957 | 0.9475  | 0.7006  | 0.0042               | 0.9977 | 1.054   | 0.7059  |

- The HRES measurements are more similar to the PR745 measurements than to the Minolta CM2500d measurements.
- The PR745 measurements are more similar to the HRES measurements than to the Minolta CM2500d measurements.
- The Minolta CM2500d measurements are more similar to the PR measurements than they are to the HRES measurements.
- The Mean and Median values are markedly different in all inter-instrument comparisons, which indicates that there are samples that produce either very similar or very dissimilar results among different devices.

These results show that the spectral data obtained with the proposed framework (HRES) are very similar in average to the data obtained with the spectroradiometer (PR745), especially in the terms of the spectral metrics, RMSE and GFC. The measurement geometry used for measuring the HRES and PR745 data is quite similar, while both instruments are different in design and measurement geometry from the spectrophotometer (Minolta CM2500d). This probably explains most of the differences found for the group of samples analyzed in this experiment between PR745 and HRES when we compare with the Minolta results, given the markedly different behavior of effect and specular samples for different illumination/observation geometries [7].

Looking at the maximum and 95 percentile results, we can conclude that there are samples that produce large inter-instrument

differences for the three devices. However, the maximum or 95 percentile results for the HRES-PR745 comparison are only slightly above the average results, which indicates a much more homogeneous group of measurements between the two 45/0 geometry devices. In addition, the effect coatings, that form a large part of the sample sets, present large spatial inhomogeneities in the reflected light pattern, with large reflection values concentrated on relatively small spots (sparkle). These sparkles contribute differently to the measured signals of the PR-745 and the HRES, because of the different ways the samples' irradiance signals are spatially integrated in the device imaging sensors. Nevertheless, the resulting inter-instrument color differences between HRES and PR-745 as summarized in Table 3 can be considered relatively small.

Based on these results, we conclude that the proposed framework for spectral image acquisition of effect coatings, at least for samples with lightness in the intermediate range in our observation/illumination conditions, can provide reflectance data with high spatial resolution and large colorimetric accuracy as compared to data obtained with a spectroradiometer operating in comparable illumination and detection geometry.

#### 4.3.3. Experiment 2: solid and effect coated samples presenting extreme lightness values

In this experiment, we analyze inter-instrument differences for a group of samples that are either very light or very dark, resulting in extreme lightness values in comparison with the samples included in Experiment 1. Thus, these samples produced either saturation or very low camera response values when measured using

the proposed work-flow and the exposure times estimated using the Color Checker Passport white as reference.

As explained in Section 2.2.2, we have introduced some adaptations in our work-flow to be able to measure the extreme samples, called the dual reference dynamic exposure time setting adaptation. Thanks to this procedure, we could capture the 28 extreme samples in Experiment 2 with acceptable values of camera responses in all the cases, even for highly specular metallic surfaces with textured coating (*effect* set). For the lighter samples, the work-flow adaptation resulted in unsaturated average camera responses within the ROI. For the darker samples, it resulted in a signal-to-noise ratio (SNR) increase of 27.7%: from 44.4 dB to 56.63 dB on average for the bands with signal below 15% of the maximum, if we compare with using the SphereOptics white for exposure time estimation without the dual reference dynamic procedure. Please note that SNR is computed as the logarithm of the ratio between the mean camera response of the samples and the mean camera response of the dark.

Fig. 10 shows plots of reflectance values for samples that have RMSE (a and b) or CIEDE00 values (c and d) close to the 95 and 5 percentiles, as representative examples of the set used in Experiment 2.

Table 4 shows the inter-instrument comparison data for the Experiment 2. The data from Table 4 supports the observations already presented in the previous subsection. For the samples used in Experiment 2, however, the group is less homogeneous, as indicated by larger standard deviation values for all metrics. The average and median inter-instrument differences are also higher than for the samples used in Experiment 1.

These differences with respect to Experiment 1 results can be explained if we consider that the samples in Experiment 2 are less homogeneous as a group in terms of lightness values. This tends to enhance the inter-instrument differences obtained. Nevertheless, we still conclude that the results obtained with the HRES are within the range of usual inter-instrument differences, especially if we compare devices that use different measurement geometry.

To further validate the proposed work-flow adaptation, we have measured the extreme samples using the SphereOptics white as reference for exposure time estimation and without the dual reference dynamic exposure time setting procedure. The results obtained were markedly more dissimilar to the PR745 measurements in average, with an increase of RMSE of 55.5%, and a 27.77% increase in CIEDE00 color difference. The maximum and 95% values supported this conclusion as well.

In Fig. 9(b and d), we can observe how the work-flow adaptation that we have introduced produces spectral reflectance curves which are slightly less smooth, very likely due to the changes in the reference reflectance values used for different bands, which can be abrupt between adjacent bands in some cases.

#### 4.4. Estimation of the spatial resolution achieved

Finally, we have also computed an estimation of the spatial resolution achieved by our capture device. The known side length in mm of the checkerboard pattern and the corresponding pixel length extracted from its image were used to estimate an approximate image resolution of 29.8  $\mu\text{m}/\text{pixel}$ . This spatial resolution is

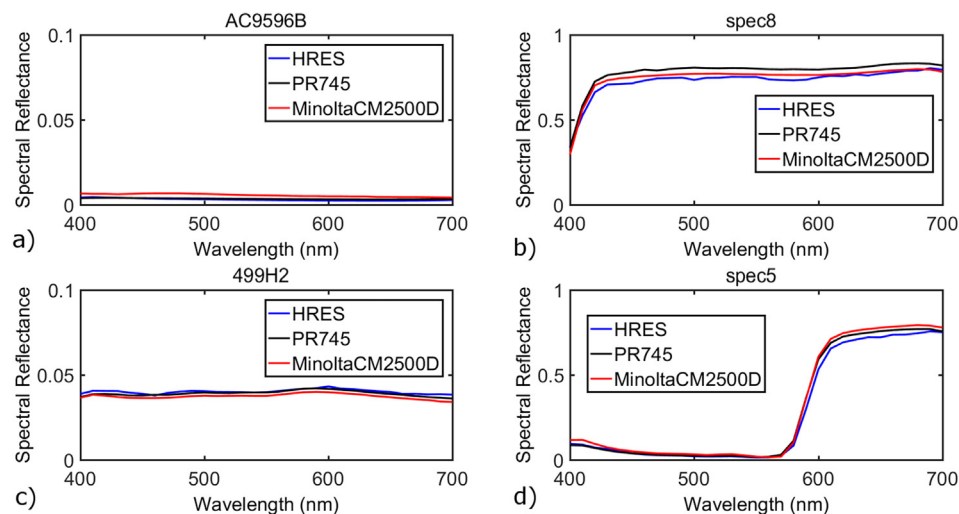


**Fig. 10.** Spectral reflectance factor for a sample with RMSE close to the 5 percentile (a), RMSE close to the 95 percentile (b), CIEDE00 close to the 5 percentile (c) and CIEDE00 close to the 95 percentile (d) in the comparison between HRES and PR745 measurements for Experiment 2 in Section 4.3. We have modified the scale in the left column figures to allow for better appreciation of the differences between measurement devices.

**Table 4**  
First order statistics for extreme samples (Experiment 2).

|               | HRES-PR745 |        |        |         | HRES-MINOLTACM2500D |        |        |         | PR745-MINOLTACM2500D |        |        |         |
|---------------|------------|--------|--------|---------|---------------------|--------|--------|---------|----------------------|--------|--------|---------|
|               | RMSE       | GFC    | CIELAB | CIEDE00 | RMSE                | GFC    | CIELAB | CIEDE00 | RMSE                 | GFC    | CIELAB | CIEDE00 |
| Mean          | 0.0162     | 0.9991 | 2.287  | 1.546   | 0.0326              | 0.9968 | 5.115  | 3.321   | 0.0243               | 0.9969 | 4.665  | 2.798   |
| Median        | 0.0129     | 0.9995 | 1.963  | 1.300   | 0.0163              | 0.9995 | 2.409  | 1.734   | 0.0084               | 0.9999 | 2.244  | 1.840   |
| STD           | 0.0179     | 0.0013 | 1.767  | 0.946   | 0.0599              | 0.0075 | 5.829  | 3.512   | 0.0565               | 0.0900 | 5.887  | 3.459   |
| Max           | 0.0617     | 0.9999 | 8.643  | 4.786   | 0.2607              | 0.9999 | 22.915 | 15.106  | 0.2722               | 1.0000 | 23.563 | 15.424  |
| Min           | 0.0004     | 0.9935 | 0.573  | 0.431   | 0.0007              | 0.9707 | 0.894  | 0.754   | 0.0006               | 0.9624 | 0.195  | 0.231   |
| 95 Percentile | 0.0526     | 0.9998 | 5.080  | 2.984   | 0.1601              | 0.9988 | 18.183 | 9.626   | 0.1138               | 1.0000 | 17.634 | 8.923   |
| 5 Percentile  | 0.0006     | 0.9971 | 0.614  | 0.650   | 0.0012              | 0.9783 | 0.955  | 0.777   | 0.0007               | 0.9779 | 0.442  | 0.374   |

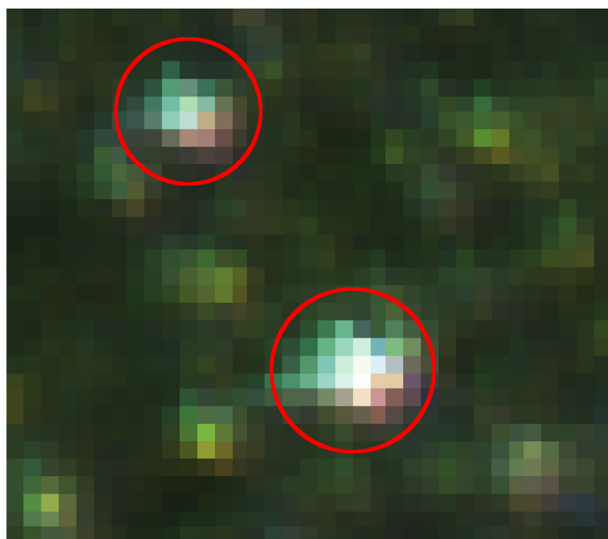


**Fig. 11.** Zoomed-out image of an effect coated sample in which we can see how the typical sparkle size exceeds one pixel. This illustrates the high spatial resolution achieved in the capture.

enough to adequately resolve the smallest spatial detail of the sparkle patterns analyzed, so that a typical sparkle point subtends more than 1 pixel always, as we show in Fig. 11.

At the usual working distance of 250 mm, the human eye would achieve a spatial resolution of 72.7  $\mu\text{m}$ , assuming the typical angular resolution limit of 1 arc minute. This shows that our capture device outperforms the human eye in terms of spatial resolution and makes it suitable to effect-coatings sample measurements.

## 5. Summary and conclusions

A novel and complete framework specially designed for high-resolution spectral imaging of effect-coated samples has been presented and validated. We have produced a comprehensive set of experiments to assess the proposed framework performance, something that to our knowledge has not been reported before within the context of spectral imaging of effect-coated samples.

For these specific samples, a high-resolution image is essential to deal with the flake-shaped pigments, called sparkle, with a size of several micrometers. An approximate image resolution of 29.8  $\mu\text{m}/\text{pixel}$  is achieved with the proposed device and framework. Because of the high spatial resolution, the distance from sample to camera is short enough to make necessary both- a focus search strategy (band by band) and an image registration procedure. We have coped with the focus search problem by shifting the object, mounted on a linear stage, instead of moving the lens. This approach allows for very precise movements for low cost as compared with autofocus lens systems. The proposed GSS-based strategy is able to achieve a significant reduction in running time while preserving sharpness in the optimal focus positions found. The importance of correctly registering the images captured for different spectral bands has also been demonstrated, applying a multi-level B-spline based registration technique which achieves sub-pixel accuracy in the registered images.

Hyperspectral measurements of effect-coated samples also have to deal with the high dynamic range produced by these samples, which exhibit extremely high and/or extremely small values of lightness. These extreme values may be due to very dark or very light base pigments, or to specific orientation of the metallic flakes. In addition, they can also be caused by significant absorption in some wavelength bands, for example, when highly saturated colors

are used as base pigments. A dual reference dynamic exposure time setting has been introduced in the framework and tested extensively. This procedure improves the match between sample and white radiance signals using combinations of two reference white samples with three target camera-response values, at the cost of increasing the temporal duration of the calibration step of the work-flow.

The final goal of the setup, to obtain reflectance measurements pixel by pixel, has been tested and it has been proven that the proposed framework is able to produce spectral reflectance measurements that are comparable to conventional point-based measurement devices if we average our spectral data over an area of similar size and position. It should be highlighted that the proposed device offers the additional advantage of providing high spatial resolution in the spectral cubes captured. The spectral and color accuracy validations of the framework have been performed using the most extensive set of effect-coated samples tested so far in hyperspectral imaging, to our knowledge, including solid colors (coatings with uniform color) and effect colors, and samples with and without extreme values for lightness.

We can identify as one limitation of our framework that it is not able to cope with the within-sample high dynamic range problem produced by the specular nature of the metallic flakes usually present in the effect-coated samples. One likely solution would be to adapt existing high dynamic range capture techniques to the proposed framework. We are contemplating this possibility for future work, although we are aware of the fact that this solution would make the work-flow running time unavoidable longer.

As prospective applications for which the proposed framework can be of interest, we can mention classification of pixels into sparkle or base pigment, color quality assessment of sparkle patterns, designing of color-difference formulae based on spectral texture information that can achieve better agreement with the human observer's color difference assessment, and (if the capture framework is extended to include different illumination/observation geometries) accurate rendering of effect coated samples in virtual reality environments.

## Funding

This research was supported by the Spanish State Agency of Research (AEI) and the Ministry for Economy, Industry and Competitiveness (MIMECO) by means of the grant number FIS2017-89258-P with European Union FEDER (European Regional Development Funds) support.

## References

- [1] E. Kirchner, G.J. van den Kieboom, L. Njo, R. Super, R. Gottenbos, Observation of visual texture of metallic and pearlescent materials, *Color Res. Appl.* 32 (2007) 256–266.
- [2] F.J. Maile, G. Pfaff, P. Reynders, Effect pigments - past, present and future, *Prog. Org. Coat.* 54 (2005) 150–163.
- [3] N. Dekker, E.J.J. Kirchner, R. Super, G.J. van den Kieboom, R. Gottenbos, Total appearance differences for metallic and pearlescent materials: contributions from color and texture, *Color Res. Appl.* 36 (2011) 4–14.
- [4] J.M. Medina, J.A. Diaz, Scattering characterization of nanopigments in metallic coatings using hyperspectral optical imaging, *Appl. Optics* 50 (2011) G47–G55.
- [5] D.B. Kim, M.K. Seo, K.Y. Kim, K.H. Lee, Acquisition and representation of pearlescent paints using an image-based goniospectrophotometer, *Opt. Eng.* 49 (2010).
- [6] A. Ferrero, E. Perales, A.M. Rabal, J. Campos, F.M. Martínez-Verdu, E. Chorro, A. Pons, Color representation and interpretation of special effect coatings, *J. Opt. Soc. Am. A* 31 (2014) 436–447.
- [7] J.M. Medina, J.A. Diaz, C. Vignolo, Fractal Dimension of Sparkles in Automotive Metallic Coatings by Multispectral Imaging Measurements, *ACS Appl. Mater. Inter.* 6 (2014) 11439–11447.
- [8] F.J. Burgos Fernández, M. Vilaseca Ricart, E. Perales Romero, E. Chorro Calderón, F.M. Martínez Verdú, J. Fernández Dorado, J.L. Álvarez Muñoz, J. Pujol Ramo, LED-based gonio-hyperspectral system for the analysis of automotive paintings, in: *AIC Interim Meeting AIC2015*, 2015, pp. 1272–1277.



- [9] M. Osumi, Evaluation and Analysis of YUTEKI-TENMOKU Visual effect of traditional ceramic applied gonio-photometric spectral imaging and confocal type laser scanning microscopy, in: AIC Interim Meeting AIC2015, 2015, pp. 147–152.
- [10] C.M. Chen, C.M. Hong, H.C. Chuang, Efficient auto-focus algorithm utilizing discrete difference equation prediction model for digital still cameras, *Ieee T Consum. Electr.* 52 (2006) 1135–1143.
- [11] S.Y. Lee, Y. Kumar, J.M. Cho, S.W. Lee, S.W. Kim, Enhanced autofocus algorithm using robust focus measure and fuzzy reasoning, *Ieee T Circ. Syst. Vid.* 18 (2008) 1237–1246.
- [12] K.R. Park, J. Kim, A real-time focusing algorithm for iris recognition camera, *Ieee Trans. Syst., Man, Cyber. Part C (Appl. Rev.)* 35 (2005) 441–444.
- [13] H.L. Shen, Z.H. Zheng, W. Wang, X. Du, S.J. Shao, J.H. Xin, Autofocus for multispectral camera using focus symmetry, *Appl. Opt.* 51 (2012) 2616–2623.
- [14] CIE, ed., Practical methods for the measurement of reflectance and transmittance (CIE Central Bureau, Vienna, 1998).
- [15] L. Shih, Autofocus survey: a comparison of algorithms, *Proc. Spie* 6502 (2007).
- [16] H.C. Xu, J.F. Liu, Y. Li, Y. Yin, C.X. Zhu, H. Lu, Autofocus using adaptive prediction approximation combined search for the fluorescence microscope in second-generation DNA sequencing system, *Appl. Opt.* 53 (2014) 4509–4518.
- [17] E. Krotkov, J.P. Martin, Range from focus, in: *Proc IEEE*, 1986, pp. 1093–1098.
- [18] J. Kiefer, Sequential minimax search for a maximum, *P Am. Math. Soc.* 4 (1953) 502–506.
- [19] G.R. Hopkinson, D.H. Lumb, Noise-reduction techniques for Ccd image sensors, *J. Phys. E Sci. Instrum.* 15 (1982) 1214–1222.
- [20] A. Darmont, High Dynamic Range Imaging: Sensors and Architectures (Washington, 2012).
- [21] P.E. Anuta, Spatial registration of multispectral and multitemporal digital imagery using fast fourier transform techniques, *Ieee Trans. Geosci. Electron. GE-8* (1970) 353–368.
- [22] L.G. Brown, A survey of image registration techniques, *Comput. Surv.* 24 (1992) 325–376.
- [23] A.A. Goshtasby, Image Registration. Principles, Tools and Methods (Advances in Computer Vision and Pattern Recognition), ed., Springer, 2012.
- [24] C. De Boor, A Practical Guide to Splines (1978).
- [25] J. Brauers, T. Aach, Geometric calibration of lens and filter distortions for multispectral filter-wheel cameras, *Ieee T Image Process* 20 (2011) 496–505.
- [26] T. Eckhard, J. Eckhard, E.M. Valero, J.L. Nieves, Nonrigid registration with free-form deformation model of multilevel uniform cubic B-splines: application to image registration and distortion correction of spectral image cubes, *Appl. Opt.* 53 (2014) 3764–3772.
- [27] J. Hernandez-Andres, J. Romero, R.L. Lee, Colorimetric and spectroradiometric characteristics of narrow-field-of-view clear skylight in Granada, Spain, *J Opt Soc Am A* 18 (2001) 412–420.
- [28] CIE, ed., Improvement to Industrial Colour-Difference Evaluation (CIE Central Bureau, Vienna, 2001).
- [29] A. Garcia-Beltran, J.L. Nieves, J. Hernandez-Andres, J. Romero, Linear bases for spectral reflectance functions of acrylic paints, *Color Res. Appl.* 23 (1998) 39–45.